CHEMISTRY OF MATERIALS

ARTICLE

pubs.acs.org/cm

Synthesis and Structural Characterization of a New Molecular Precursor for $BaHfO_3$: A Simple Approach to Eu-Based Phosphors

Anna Drąg-Jarząbek, Magdalena Kosińska, Łukasz John, Lucjan B. Jerzykiewicz, and Piotr Sobota*

Faculty of Chemistry, University of Wrocław, 14 F. Joliot-Curie, 50-383 Wrocław, Poland

S *Supporting Information*

ABSTRACT: A single-source molecular precursor $[Ba_4Hf_2(\mu_6\text{-}O)(\mu_3,\eta^2\text{-}OR)_8(\mu\text{-}OR)_2(\mu\text{-}ROH)_4Cl_4]$ (ROH = $CH_3OCH_2CH_2OH$) for mixed-metal oxide materials was prepared via elimination of the cyclopentadienyl ring from Cp_2HfCl_2 as CpH, in the presence of $Ba(OR)_2$ in an alcohol ROH as a source of protons. The precursor was characterized by elemental analysis, infrared (IR) and nuclear magnetic resonance (NMR) spectroscopy, and single-crystal X-ray structural analysis. This complex undergoes thermal decomposition at 800 °C to a $BaCl_2/BaHfO_3$ mixture. After barium dichloride has been leached from the raw powder using deionized water, the resulting particles are of submicrometer size (30−50 nm). Preliminary studies of barium hafnate doped with Eu^{3+} sintered at 900 °C showed that a dominant luminescence band belongs to the strong electric dipole transition $^5D_0 \rightarrow {}^7F_2$.

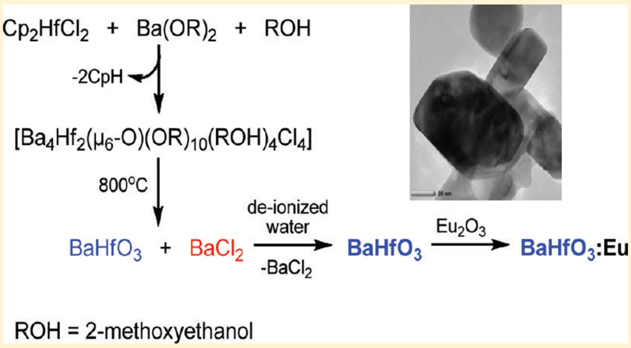

KEYWORDS: barium hafnate, perovskite, single-source precursor (SSP), phosphors

INTRODUCTION

Highly phase-pure $BaHfO_3$ nanopowders that can play a role as matrices for luminescent doping are extremely desirable. Barium hafnate is an attractive host lattice for new X-ray phosphors, which are much more effective than the phosphors currently used in radiology and computed tomography (such as BaFBr:Eu, CsI:Tl, $CdWO_4$, Gd_2O_2S:Tb, etc.).[1] Its attractiveness lies in the higher photofraction and absorption coefficient in the range of medical X-rays.[2] In the literature, there are numerous approaches to the synthesis of barium-based perovskite materials. For example, Thomas et al. synthesized barium hafnate using an autoignition modified combustion technique at 1650 °C for 2 h and a $Ba(NO_3)_2/HfCl_4$/citric acid system.[3] Zhang and Evetts prepared monophasic $BaHfO_3$ powders using a spray drying method and then calcinated raw materials at 1150 °C for ∼20 h.[4] In turn, Wang et al. obtained barium hafnate powders by mixing barium nitrate and hafnium(IV) chloride with ammonium oxalate aqueous solution at 800 °C for 2 h.[5] Intensive research in the field of ceramic materials has triggered an unusual interest in alkoxo metal derivatives resulting from their rich structural diversity and potential practical applications as versatile single-source precursors for the preparation of nanosized particles.[6,7] Moreover, alkoxo groups are quite easy to remove during thermal treatment for conversion to appropriate oxide materials.[8] Among many possible heterobimetallic complexes, those which contain barium−hafnium compounds have become a cornerstone of advances in new materials. Barium-containing compounds are slightly scarcer, although some interesting examples have been published recently. For example, Veith and co-workers reported some well-defined barium/Group 4 metal complexes $[BaZr_2(O^tBu)_{10}]$,[9] $[Ba_2Zr(O^tBu)_8(HO^tBu)]\cdot 2THF$,[9] $[BaTi_3(O^iPr)_{14}]$,[10] and $[\{Cd(O^iPr)_3\}Ba\{Hf_2(O^iPr)_9\}]_2$.[11] Also, Hubert−Pfalzgraf et al. reported some very interesting barium−copper and barium−yttrium species, such as $[YBa_2(HFIP)_7(THF)_3]$, $[BaCu(HFIP)_4(DME)_2]$, $[Y_2Ba(HFIP)_4(thd)_4]$, $[BaCu_2(HFIP)_4(thd)_2]$, and $[YCu(HFIP)(thd)]$ (where HFIP = 1,1,1,3,3,3-hexafluoro-2-propoxide; thdH = 2,2,6,6-tetramethyl-3,5-heptanedione).[12] In our research group, we have also synthesized a family of barium-based heterometallic $[Ba\{(\mu\text{-ddbfo})_2MR_2\}_2]$ (ddbfoH = 2,3-dihydro-2,2-dimethylbenzofuran-7-ol; M = Al, Ga; R = Me, Et) compounds.[13] Recently, we described our studies on titanium and zirconium metallocenes and showed these to be attractive and inexpensive precursors for an extensive range of novel molecular and supramolecular materials.[14] Our synthetic method comprises elimination of the cyclopentadienyl ring from Cp_2MCl_2 (M = Ti, Zr) as CpH in the presence of $Ca(OR)_2$ and an alcohol ROH (ROH = $CH_3OCH_2CH_2OH$) as a source of protons. Herein, we report results of our further studies and present the synthesis of this new barium−hafnium $[Ba_4Hf_2(\mu_6\text{-}O)(\mu_3,\eta^2\text{-}OR)_8(\mu\text{-}OR)_2(\mu\text{-}ROH)_4Cl_4]$ (**1**) under mild conditions. The unique cluster structure of **1** makes it an excellent single-source precursor (SSP) for the generation of $BaHfO_3$ perovskite luminescence powders activated with Eu^{3+} ions.

Received: June 1, 2011
Revised: August 2, 2011
Published: September 02, 2011

EXPERIMENTAL SECTION

General Procedures and Methods. Reaction was conducted under nitrogen atmosphere using standard Schlenk techniques. Solvents were prepared as follows: toluene, distilled from Na/benzophenone; hexanes, distilled from P_2O_5. Barium (pieces, 99%), bis(cyclopentadienyl)hafnium(IV) dichloride (Cp_2HfCl_2 powder, 98%), 2-methoxyethanol (anhydrous liquid, 99.8%), and europium(III) oxide (Eu_2O_3 powder, 99.9%) were purchased from Aldrich and used without further purification. Microanalyses were conducted with an elemental analyzer (Model 2400 CHNS Vario EL III, Elementar). The concentration of metal ions was determined by the ICP technique, using an ARL model 3410 sequential spectrometer (Fisons Instruments). Infrared (IR) spectra were recorded on a Bruker Model 66/s FT-IR spectrophotometer in Nujol mulls (peaks at 2925, 2854, 1462, and 1377 cm^{-1} belong to Nujol). NMR spectra were obtained on a Bruker Avance 500 MHz spectrometer. Mass spectroscopy (MS) analyses were recorded on a micrOTOF-Q ESI mass spectrometer (Bruker) and gas chromatography/mass spectroscopy (GC/MS) on a gas chromatograph with a mass detector (Hewlett–Packard, Model HP 5971A). Thermogravimetric analyses (TGAs) were performed under a nitrogen and air atmosphere, using a SETSYS 16/18 system manufactured by Setaram with a heating rate of 5 °C min^{-1}. Thermal decompositions were performed using a Model NT 1313 furnace with thermostat KXP3+ production (NEOTHERM). Samples were thermolyzed in atmospheric air. The thermolyzed products were characterized recording powder X-ray diffraction (XRD) patterns with a Bruker D8 Advance diffractometer equipped with a copper lamp ($\lambda_{Cu\,K\alpha}$ = 1.5418 Å). Standard measurements were done for 2θ = 10°–90° with a 2θ step of 0.016° and a counting time of 0.3 s. The morphology of powders was tested with high-resolution transmission electron microscopy (TEM), using a FEI Tecnai G^2 20 X-TWIN microscope operating at 200 kV and providing 0.25-nm resolution and equipped with an microanalysis EDAX and scanning electron microscopy (SEM) using a Hitachi S-3400N microscope equipped with an EDS Thermo Noran System SIX. Nitrogen porosimetry was performed at 77 K on a Micromeritics ASAP 2020 M system. The specific surface area (S_{BET}) was calculated by the Brunauer–Emmett–Teller (BET) method. The mesopore size distribution was analyzed by the Barrett–Joyner–Halenda (BJH) method with a desorption branch. Pore size distributions were calculated using the BJH model based on nitrogen desorption isotherms. Photoluminescence spectra were recorded using a Model FSL920 spectofluorimeter (Edinburgh Instruments) with a 450-W xenon lamp and a photomultiplier tube (PMT) operating at a range of 185–870 nm. The luminescence spectra were taken with a resolution of 0.2 nm.

Scheme 1. Synthesis of 1

$$Cp_2HfCl_2 + Ba(OR)_2 + ROH \xrightarrow[\text{toluene, r.t.}]{-2CpH} [Ba_4Hf_2(\mu_6\text{-}O)(OR)_{10}(ROH)_4Cl_4]$$

(**1**)

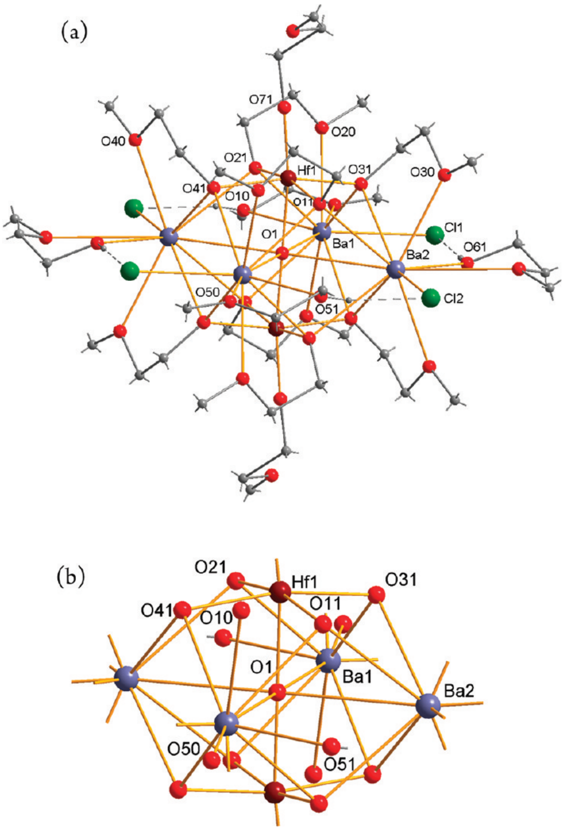

Figure 1. (a) Molecular structure of **1**. (b) Octahedral $Ba_4Hf_2(\mu_6\text{-}O)(\mu_3\text{-}O)_8$ core.

Synthesis of $[Ba_4Hf_2(\mu_6\text{-}O)(\mu_3,\eta^2\text{-}OR)_8(\mu\text{-}OR)_2(\mu\text{-}ROH)_4Cl_4]$ (1). A Schlenk flask was charged with Cp_2HfCl_2 (1.00 g, 2.63 mmol), $Ba(OCH_2CH_2OCH_3)_2$ (1.52 g, 5.26 mmol), 20 mL of $CH_3OCH_2CH_2OH$ (19.30 g, 0.25 mol), and toluene $C_6H_5CH_3$ (20 mL). The mixture was vigorously stirred for 4 h. The resulting yellow solution was filtered, concentrated under vacuum to 20 mL, and left to crystallize at room temperature. After a few hours, colorless crystals were collected, washed with *n*-hexane (3 × 5 mL), and dried under vacuum. The filtrate was reduced in volume to 10 mL and gave, after overnight standing, another portion of crystalline material. Overall yield: (2.13 g, 1.00 mmol, 76%). Calcd for $C_{42}H_{102}O_{29}Cl_4Hf_2Ba_4$ (MW, 2119.38): C, 23.80; H, 4.85; Cl, 6.69; Hf, 16.84; Ba, 25.92. Found: C, 23.76; H, 4.83; Cl, 6.66; Hf, 16.78; Ba, 25.86. IR (cm^{-1}, Nujol mull): 3133 (s), 2925 (br), 2766 (w), 2717 (w), 1618 (w), 1457 (vs), 1377 (s), 1366 (m), 1344 (m), 1290 (m), 1247 (s), 1201 (m), 1169 (vs), 1116 (vs), 1070 (vs), 1023 (vs), 934 (w), 900 (vs), 835 (s), 710 (m); 552 (m); 452 (w), 406 (vs), 370 (vs), 316 (vs), 2 72 (m), 237 (m), 152(s). ^1H NMR ($CDCl_3$, 298 K, ppm): δ = 5.14 (s, 4H, $HOCH_2CH_2OCH_3$), 4.14 (br, 16H, $OCH_2CH_2OCH_3$), 4.01 (t, 4H, $OCH_2CH_2OCH_3$, J_{H-H} = 5 Hz), 3.71 (t, 8H, $HOCH_2CH_2OCH_3$, J_{H-H} = 5 Hz), 3.57 (br, 16H, $OCH_2CH_2OCH_3$), 3.52 (s, 12H, $HOCH_2CH_2OCH_3$) 3.48 (s, 24H, $OCH_2CH_2OCH_3$), 3.45 (t, 8H, $HOCH_2CH_2OCH_3$, J_{H-H} = 5 Hz), 3.28 (t, 4H, $OCH_2CH_2OCH_3$, J_{H-H} = 5 Hz), 3.23 (s, 6H, $OCH_2CH_2OCH_3$). $^{13}C\{^1H\}$ NMR ($CDCl_3$, 298 K, ppm): δ = 77.43 (s, 4C, $HOCH_2CH_2OCH_3$), 76.48 (s, 2C, $OCH_2CH_2OCH_3$), 73.88 (s, 8C, $OCH_2CH_2OCH_3$), 67.72 (s, 2C, $OCH_2CH_2OCH_3$), 64.64 (s, 4C, $HOCH_2CH_2OCH_3$), 61.01 (s, 8C, $OCH_2CH_2OCH_3$), 59.8 (s, 8C, $OCH_2CH_2OCH_3$), 59.64 (s, 4C, $HOCH_2CH_2OCH_3$), 58.62 (s, 2C, $OCH_2CH_2OCH_3$). GC/MS: CpH, CpH dimer (traces). MS, *m*/*z* = 1779.9 $[Ba_4Hf_2(\mu_6\text{-}O)(OCH_2CH_2OCH_3)_{10}Cl_3]^+$, 1572.0 $[Ba_3Hf_2(\mu_6\text{-}O)(OCH_2CH_2OCH_3)_{10}Cl_1]^+$, 1174.9 $[Ba_2Hf_2(\mu_6\text{-}O)(OCH_2CH_2OCH_3)_5(CH_3OCH_2CH_2OH)_2]^+$, 872.4 $[Ba_4Hf_2(\mu_6\text{-}O)(OCH_2CH_2OCH_3)_{10}Cl_2]^{2+}$, 768.5 $[Ba_3Hf_2(\mu_6\text{-}O)(OCH_2CH_2OCH_3)_{10}]^{2+}$, 624.5 $[Ba_2Hf_2(\mu_6\text{-}O)(OCH_2CH_2OCH_3)_8]^{2+}$.

X-ray Determinations of Structures. The crystal was mounted on glass fibers and then flash-frozen to 100(2) K (Oxford Cryosystem−Cryostream Cooler). Preliminary examination and intensity data collections were carried out on a Kuma Model KM4CCD κ-axis diffractometer with graphite-monochromated Mo Kα radiation. All data were corrected for Lorentz, polarization, and absorption effects. Data reduction and analysis were carried out with the Kuma Diffraction programs.[15] The structure was solved by direct methods and refined by the full-matrix least-squares method on all F^2 data, using the SHELXTL software.[16] Carbon-bonded hydrogen atoms were included in calculated positions and refined in the riding mode using SHELXTL default parameters. Other hydrogen atoms were located in a difference Fourier map, and refined with distance restraints of O−H. The coordinated $CH_3OCH_2CH_2OH$ and $CH_3OCH_2CH_2O^-$ molecules were partially disordered, and they were refined in two positions. The final difference Fourier map was essentially featureless, with the largest peaks being 2.6 and −1.52 e Å^{-3} near Ba^{2+} ions and the disordered ligand.

Table 1. Crystallographic Data for 1

property	value
empirical formula	$C_{42}H_{102}Ba_4Cl_4Hf_2O_{29}$
M	2119.38
cryst sys	triclinic
space group	$P\bar{1}$
temperature (K)	100
a (Å)	12.669(4)
b (Å)	12.880(5)
c (Å)	13.532(4)
α (deg)	106.70(4)
β (deg)	103.66(4)
γ (deg)	113.54(5)
V (Å^3)	1777.4(17)
Z	1
radiation type	Mo Kα
cryst size (mm^3)	0.21 × 0.12 × 0.10
μ (mm^{-1})	5.31
T_{min}, T_{max}	0.714, 0.919
No. of measured, independent and observed [$I > 2s(I)$] reflections	26169, 8528, 7191
R_{int}	0.026
$R[F^2 > 2s(F^2)]$, $wR(F^2)$, S	0.027, 0.067, 1.05
No. of reflections	8528
No. of parameters	375
No. of restraints	1
H-atom treatment	H atoms treated with a mixture of independent and constrained refinement
$D\rho_{max}$, $D\rho_{min}$ (e Å^{-3})	2.60, −1.52

Preparation of $BaHfO_3$. In a typical procedure, cluster **1** was heated at 800 °C for 1 h in an air atmosphere at a heating rate of 5 °C min^{-1}. After decomposition, the product was identified using powder XRD. In the next step, raw powder was leached using deionized water and then dried in an oven at 120 °C for 1 h. The morphology and elemental composition of pure $BaHfO_3$ particles has been investigated using transmission electron microscopy−energy-dispersive spectroscopy (TEM-EDS)/scanning electron microscopy−energy-dispersive spectroscopy (SEM-EDS) methods. Carbon, hydrogen, and chlorine contaminations were examined by elemental analysis and Fourier transform infrared (FT-IR) spectroscopy.

RESULTS AND DISCUSSION

Synthesis and Molecular Structure of 1. Reaction of Cp_2HfCl_2 with 2 equiv of $Ba(OR)_2$ and an excess of ROH (ROH = 2-methoxyethanol) in toluene at room temperature gave the colorless cyclopentadienyl-free heterometallic $[Ba_4Hf_2(\mu_6\text{-}O)(\mu_3,\eta^2\text{-}OR)_8(\mu\text{-}OR)_2(\mu\text{-}ROH)_4Cl_4]$ (**1**, 76%) cluster (see Scheme 1). The choice of functionalized alcohol was

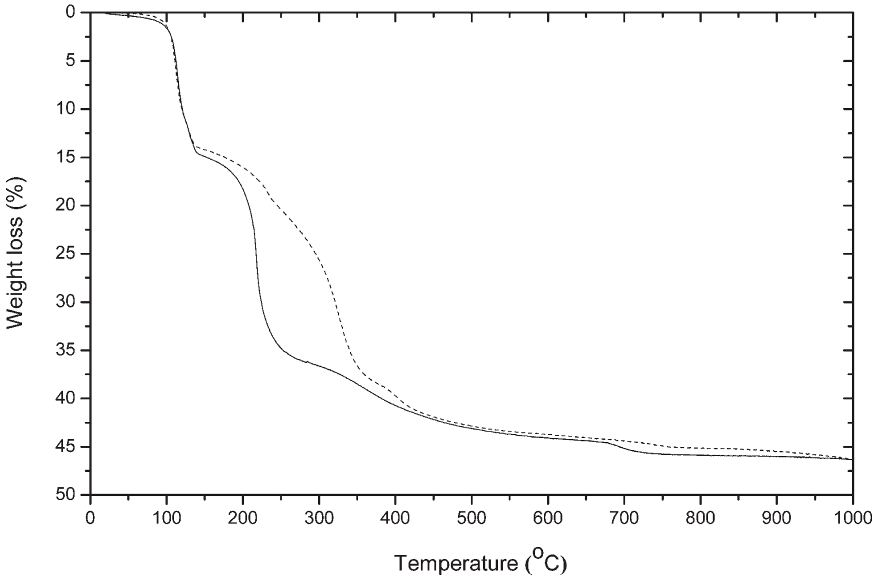

Figure 2. TGA curves of **1** performed in (—) air and (- - -) N_2 atmospheres.

Table 2. Selected Bond Lengths and Angles for 1[a]

Bond Lengths

bond	length (Å)	bond	length (Å)
Hf(1)−O(1)	2.027(1)	Ba(1)−O(41)	2.939(3)
Hf(1)−O(71)	2.052(6)	Ba(1)−O(50)	3.158(3)
Hf(1)−O(11)	2.108(3)	Ba(1)−Cl(1)	3.085(2)
Hf(1)−O(31)	2.111(3)	Ba(2)−O(1)	3.154(2)
Hf(1)−O(21)	2.115(3)	Ba(2)−O(61)	2.773(3)
Hf(1)−O(41)	2.116(3)	Ba(2)−O(40^i)	2.789(4)
Ba(1)−O(1)	3.151(2)	Ba(2)−O(31)	2.811(3)
Ba(1)−O(51)	2.727(3)	Ba(2)−O(41^i)	2.811(4)
Ba(1)−O(20^i)	2.770(3)	Ba(2)−O(30)	2.815(4)
Ba(1)−O(10)	2.806(4)	Ba(2)−O(11)	2.934(3)
Ba(1)−O(21^i)	2.816(3)	Ba(2)−O(21^i)	2.941(3)
Ba(1)−O(11)	2.818(3)	Ba(2)−O(60)	3.243(4)
Ba(1)−O(31^i)	2.938(4)	Ba(2)−Cl(2)	3.085(2)

Bond Angles

bond	angle (°)	bond	angle (°)
O(1)−Hf(1)−O(71)	176.87(16)	O(21)−Hf(1)−O(41)	88.56(11)
O(1)−Hf(1)−O(11)	84.71(10)	O(51)−Ba(1)−O(20^i)	71.81(11)
O(71)−Hf(1)−O(11)	94.5(2)	O(51)−Ba(1)−O(10)	71.46(11)
O(1)−Hf(1)−O(31)	84.39(8)	O(20^i)−Ba(1)−O(10)	132.47(9)
O(71)−Hf(1)−(O31)	92.58(18)	O(51)−Ba(1)−O(21^i)	74.43(11)
O(11)−Hf(1)−O(31)	89.89(11)	O(20^i)−Ba(1)−O(21^i)	60.33(9)
O(1)−Hf(1)−O(21)	83.74(10)	O(10)−Ba(1)−O(21^i)	133.17(9)
O(71)−Hf(1)−O(21)	97.0(2)	O(51)−Ba(1)−O(11)	74.93(9)
O(11)−Hf(1)−O(21)	168.45(11)	O(51)−Ba(1)−Cl(1)	122.99(8)
O(31)−Hf(1)−O(21)	89.27(11)	O(10)−Ba(1)−Cl(1)	86.59(8)
O(1)−Hf(1)−O(41)	83.82(8)	O(11)−Ba(1)−Cl(1)	136.91(7)
O(71)−Hf(1)−O(41)	99.22(18)	O(51)−Ba(1)−O(1)	111.37(8)
O(11)−Hf(1)−O(41)	89.91(11)	O(20^i)−Ba(1)−O(1)	109.73(8)
O(31)−Hf(1)−O(41)	168.17(11)	Cl(1)−Ba(1)−O(1)	125.63 (4)

[a] Symmetry code: (i) = $x + 1, -y + 1, -z + 1$.

Scheme 2. Thermal Transitions of 1

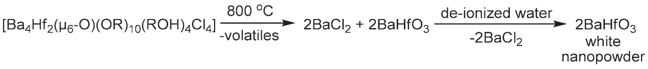

$$[Ba_4Hf_2(\mu_6\text{-}O)(OR)_{10}(ROH)_4Cl_4] \xrightarrow[\text{-volatiles}]{800\ ^\circ C} 2BaCl_2 + 2BaHfO_3 \xrightarrow[\text{-}2BaCl_2]{\text{de-ionized water}} \underset{\text{white nanopowder}}{2BaHfO_3}$$

particularly suited for forming a small aggregate, because the two donor oxygen atoms can be tethered between metal atoms in $\mu_3-\eta^2$, $\mu-\eta^2$, $\mu_3-\eta^1$, or $\mu-\eta^1$ modes. Deprotonation of its hydroxide group creates a bidentate monoanion. Cluster **1** gave a correct microanalysis and was characterized by spectroscopic studies and further confirmed by single-crystal XRD analysis (see Figure 1, and Tables 1 and 2). The central $Ba_4Hf_2(\mu_6\text{-}O)(\mu_3\text{-}O)_8$ core of **1** can be described as an octahedron with six metal centers and a μ_6-oxo encapsulated oxygen atom residing at the central position and with each of the triangular faces being capped by a μ_3-oxygen atom of the alkoxide group. The most probable sources of the O^{2-} anion are alkene/ether elimination reactions or adventitious hydrolysis.[17,18] Hf and Ba atoms occupy axial and equatorial positions, respectively. Each of the barium coordination spheres is completed by terminal chlorine ligands with a ClO_8 donor set. The Ba−O_{oxo} distances (see Table 2) are in the range of 3.151(2)−3.154(2) Å; for Hf−O_{oxo}, it is 2.027(1) Å. The Ba−Cl bond distance is 3.085(2) Å. In turn, the Ba−O_{alkoxo}, Ba−O_{ether}, and Hf−O_{alkoxo} bond distances are in the range of 2.727(3)−2.941(3) Å, 2.770(3)−3.243(4) Å, and 1.909(5)−2.116(3) Å, respectively. All bond distances and angles are comparable to those reported in the literature.[9−13]

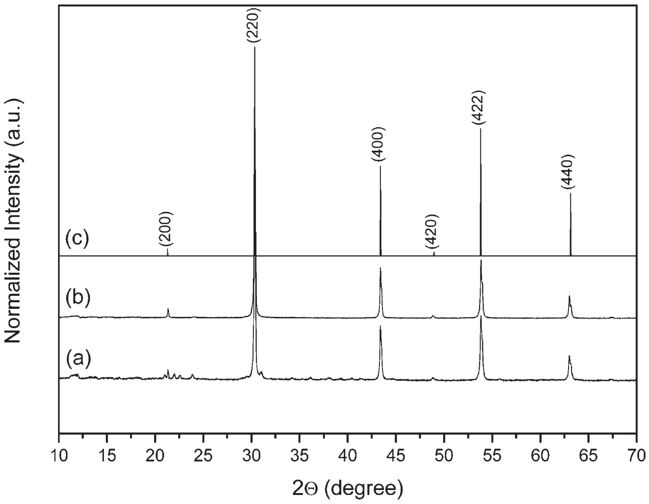

Figure 3. Powder XRD patterns: (a) mixture of $BaCl_2$ and $BaHfO_3$ (pattern a), $BaHfO_3$ (pattern b), and $BaHfO_3$ (JCPDS Powder Diffraction File Card No. 24-0102) (pattern c).

Thermal Decomposition of 1 and Characterization of $BaHfO_3$. Alkoxide complexes generally are highly moisture-sensitive. Because of this, the thermal decomposition of **1** was investigated first using TGA analysis under an air and nitrogen atmosphere (see Figure 2). No signs of sublimation were observed. Thermolysis clearly indicates that **1**, when heated from room temperature up to 950 °C within 1.5 h (step = 10 °C/min), undergoes multistep transformations. The subsequent weight losses observed in TGA experiments clearly correspond to a mixture of $BaCl_2$ and $BaHfO_3$ (see Scheme 2) in a 1:1 molar ratio (weight losses under N_2 and air atmospheres are 45.16% and 45.88%, respectively; calculated weight loss is 46.02%). Unfortunately, the subsequent weight losses observed in TGA experiments do not correspond with the weight losses predicted when a specific number of ligands is liberated. Additional TG-FTIR studies of the gas phase have shown that its volatiles did not contain any metal−ligand moieties. Moreover, in the FT-IR spectra of the volatile products, only CO, CO_2, and simple hydrocarbons were detected. It is well-known that the thermal decomposition of **1** containing a bidentate ligand is a much more complex and extended process, compared to molecular precursors with monodentate RO^- (R = Me, Et, ^{i}Pr) groups. This period of time is necessary to fully decompose and remove organic contamination from the oxide material. TGA studies of **1** performed in N_2 atmosphere clearly show that precursor is not fully decomposed at 800 °C. Thus, elemental analysis of the resulting powder indicates the presence of residues of C and H contaminations.

Powder XRD patterns of both a mixture of $BaCl_2/BaHfO_3$ (raw powder) and pure $BaHfO_3$ derived from **1** are shown in Figures 3a and 3b. After decomposition, the $BaCl_2/BaHfO_3$ molar ratio was 1 ± 0.02. In order to obtain pure $BaHfO_3$, the raw powder sintered at 800 °C was washed twice with deionized water to leach out barium dichloride (Figure 3a; see Scheme 2)

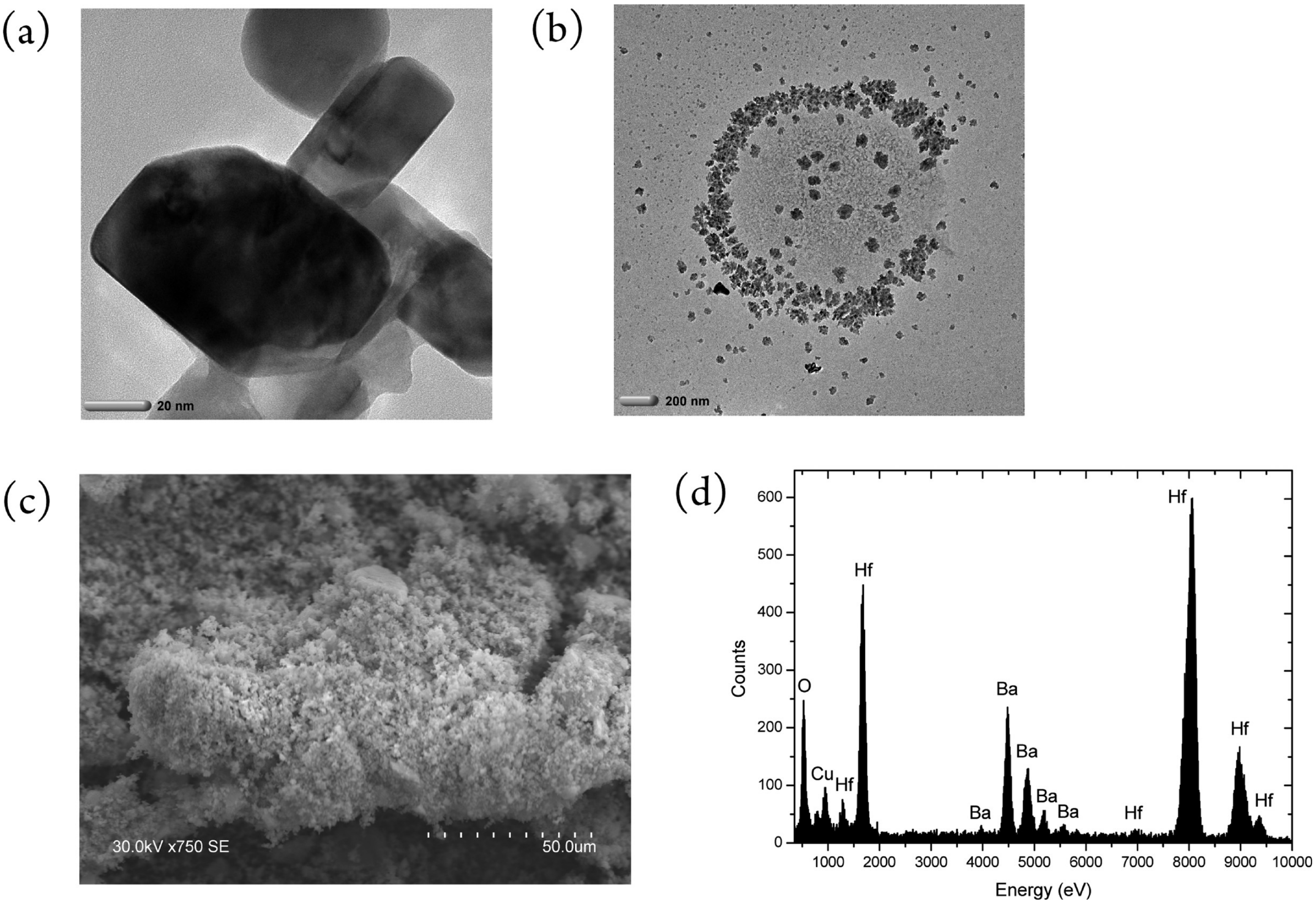

Figure 4. Characterization of $BaHfO_3$: (a) and (b) TEM images, (c) SEM image, and (d) EDS spectrum (copper content are derived from the high-purity conducting Cu/C plate).

(yield calcd for $BaHfO_3$ = 98%). All the peaks in the pattern shown in Figure 3b are indexed for the cubic structure (*Pm*3*m*) and are in agreement with the reported standard value for cubic barium hafnate (see Figure 3c).[19−21] Crystalline impurities, such as $BaCO_3$ or HfO_2, were not detected by powder XRD. The average size of grains (35−70 nm) was calculated by the Debye−Scherrer equation for the half-width of the three most intense peaks (designated based on the line extending with appropriate diffractive 2θ angles: 30.4°, 43.4°, 53.8°). In turn, the presence of barium dichloride was confirmed by elemental analysis and FT-IR spectra. The bands at 109 and 85 cm^{-1} are assigned to the υ(Ba−Cl) vibrational modes and peak at 1611 cm^{-1} is characteristic for stretching vibration of the υ(O−H) from water molecules of the hygroscopic barium chloride. Furthermore, the υ(Ba−O) band is observed at 133 cm^{-1}. Moreover, the appearance of the peaks at 857 and 544 cm^{-1} are assigned to symmetric and asymmetric vibrations of HfO_6 octahedra within the $BaHfO_3$ structure (see Figures S1 and S2 in the Supporting Information).[19−21] The presence of barium carbonates was excluded using FT-IR, powder XRD analysis for $2\theta < 10°$, and elemental analysis.

The TEM−EDS and SEM-EDS analyses were performed on several grains. The EDS spectrum (Figure 4d) of $BaHfO_3$ confirmed the 1:1 ratio of the barium and hafnium metals and the absence of halides in the oxide product. TEM studies on the powder morphology of the pure $BaHfO_3$ showed that the particles are of submicrometer size, in the range of 30−50 nm (see Figure 4).

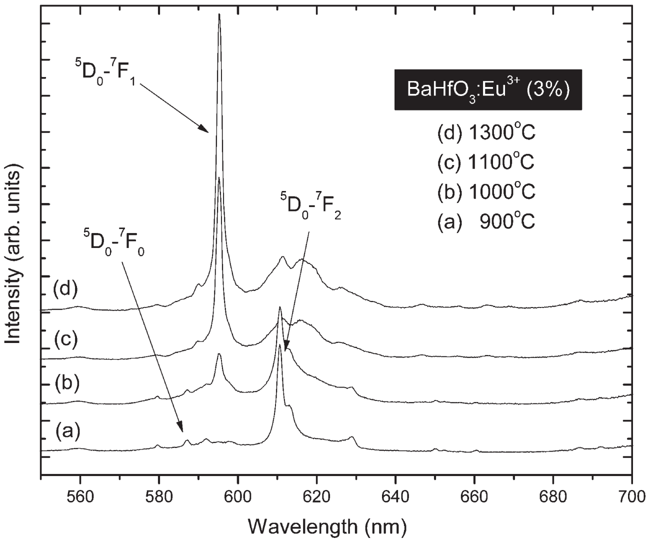

Figure 5. Emission spectra of $BaHfO_3$:Eu^{3+} sintered at different temperatures (λ_{exc} = 260 nm).

The particles are of regular cuboidal shape with curved grain boundaries. The resulting solid $BaHfO_3$ is essentially nonporous to molecular nitrogen and has a low Brunauer−Emmett−Teller (BET) surface area of 10.6 m^2 g^{-1}, which was confirmed by

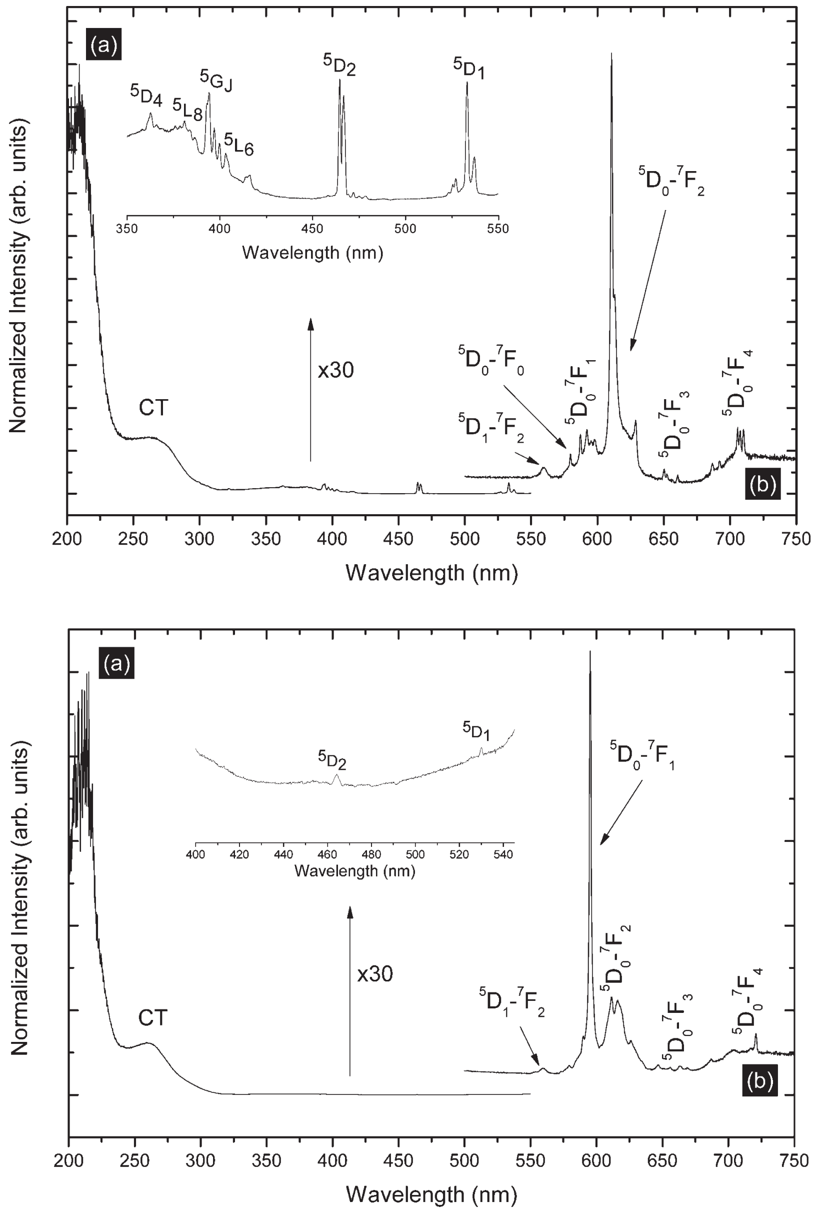

Figure 6. (top) Photoluminescence spectra of $BaHfO_3:Eu^{3+}$ sintered at 900 °C: (a) excitation spectrum (λ_{em} = 610.4 nm) and (b) emission spectrum (λ_{exc} = 260 nm). (bottom) Photoluminescence spectra of $BaHfO_3:Eu^{3+}$ sintered at 1300 °C: (a) excitation spectrum (λ_{em} = 595.6 nm) and (b) emission spectrum (λ_{exc} = 260 nm).

physisorption analysis (see Figures S3−S5 in the Supporting Information). A lack of porosity is favorable in phosphors. Pores in the microstructures of ceramics can strongly scattering incident lights, which is responsible for opaque of the resulting material.[22]

Luminescence Studies of $BaHfO_3$:Eu. Luminescence studies of Eu-doped barium hafnate were performed. A sample of $BaHfO_3$ with Eu_2O_3 was ground in a mortar with acetone. The Eu^{3+} concentration was 3 mol %, with respect to Ba. $BaHfO_3$:Eu was sintered at different temperatures in the range from 900° to 1300 °C in air. It can be seen that emission spectra (Figure 5) change significantly and increase with sintering temperature. At 900 °C, a dominant band belongs to the electric dipole transition ($^5D_0 \rightarrow {}^7F_2$), whereas, at 1300 °C, it is assigned to the magnetic dipole transition ($^5D_0 \rightarrow {}^7F_1$).[23] It is well-known that $^5D_0-{}^7F_1$ is a magnetic dipole transition that does not change with the crystal field strength around the Eu^{3+} ions and dominates emission spectrum when the Eu^{3+} ions located at a site of inversion symmetry. The $^5D_0-{}^7F_{2,4}$ are electric-dipole-induced transitions hypersensitive to the local symmetry around Eu^{3+} ions. When the Eu^{3+} ions occupy noninversion symmetry sites, the $^5D_0-{}^7F_2$ transition dominates emission spectrum. Moreover, increasing distortion of the local field around Eu^{3+} ions increases its intensity.[24] In the cubic cell of barium hafnate, Ba^{2+} ions occupy the center of the cube and are surrounded by 12 O^{2-} ions, while Hf(IV) ions are positioned in the corners of the cube and enclosed by six O^{2-} ligands.[25] Because of the ionic radius difference of barium (0.161 nm), hafnium (0.071 nm), and Eu^{3+} (0.095 nm), we cannot definitely determine which metal site is substituted by Eu^{3+} ions,[26] but because of the much smaller size difference between Eu^{3+} and Hf^{4+} than Ba^{2+}, the Eu^{3+} ions are expected to enter the host into Hf^{4+} sites in the HfO_6 octahedra.[27]

Since the dominant emission in the spectrum of the sample sintered at 900 °C (Figure 5a) is the $^5D_0-^7F_2$ electric dipole transition and $^5D_0-^7F_0$ transition strictly parity-forbidden by the selection rule also appears on the spectrum, it can be concluded that EuO_6 octahedra in $BaHf_{1-x}Eu_xO_3$ host lattice are distorted and there is a lack of inversion symmetry at the Eu^{3+} site. Figure 5 shows that increasing the sintering temperature decreases the intensity of the $^5D_0-^7F_2$ electric dipole transition and the rising intensity of the $^5D_0-^7F_1$ magnetic dipole transition at the same time. Also, the forbidden $^5D_0-^7F_0$ transition decreases and disappears at 1300 °C (see Figure 5d). It leads to the conclusion that the distortion of EuO_6 octahedra decreases and local symmetry around the Eu^{3+} ion increases as the sintering temperature increases.

At 900 °C, a dominant band that belongs to the electric dipole transition ($^5D_0 \rightarrow ^7F_2$) is observed, whereas, at 1300 °C, it is assigned to the magnetic dipole transition ($^5D_0 \rightarrow ^7F_1$).[25] The emission spectrum (top of Figure 6b) upon excitation of the charge transfer band of Eu^{3+} consists of narrow lines with peaks at 559.4, 579.6, 592, 610.4, 650, and 705 nm, appearing as a result of $^5D_1-^7F_2$ and $^5D_0-^7F_{0,1,2,3,4}$ transitions of Eu^{3+}, respectively. The most significant luminescent line is related to the electric dipole transition $^5D_2-^7F_2$ which, together with the presence of the forbidden $^5D_0-^7F_0$ transition and the number of lines, indicates that the Eu^{3+} environment is not centrosymmetric.[26] The excitation spectrum (shown in the top portion of Figure 6a) corresponding to the peak at 610.6 nm presents a series of narrow lines in the range of 350−550 nm, which is assigned to 4f−4f transitions of Eu^{3+} ions. This confirms the noncentrosymmetric environment around the activator, although the very low intensity of the f−f transitions suggests that the symmetry around Eu^{3+} is high.[26] Broad-band peaking at 260 nm is attributed to a $Eu^{3+}-O^{2-}$ charge transfer (CT) transition. The lower spectra (bottom of Figure 6) show photoluminescence of $BaHfO_3:Eu^{3+}$ sintered at 1300 °C. The most-intensive emission line (peak at 590.6 nm) is assigned to a $^5D_0-^7F_1$ magnetic dipole transition, which is partially allowed if the activator ion has a centrosymmetric environment. The presence of forbidden transitions indicates that the Eu^{3+} surrounding is not purely centrosymmetric. Their low intensity suggests that distortion around the activator is not very significant.[26] Also, the excitation spectrum, despite the CT transition band, exhibits extremely weak lines attributable to 4f−4f transitions.

CONCLUSIONS

We have, for the first time, presented a novel, efficient, and easy-to-scale-up synthetic pathway to well-defined $BaHfO_3$ nanoparticles at very low temperature and with simple control of the process parameters, high efficiency, and high yield. The heterometallic precursor **1** of barium and hafnium was obtained via simple chemical reaction of Cp_2HfCl_2 with $Ba(OR)_2$, using a molar ratio of 1:2 in the presence of ROH under mild conditions. Our method is also relatively inexpensive, compared to using hafnium oxide and barium carbonate starting materials in the previously favored solid-state synthesis of barium hafnate. Furthermore, solid-state methods require the use of high temperature, long reaction times, and low chemical uniformity, and they generally result in large particles. We have also shown that $BaHfO_3$ derived from a molecular precursor **1** might be an attractive host lattice for Eu-doped phosphors. It is worth noting that the strong emission derived from the $^5D_0-^7F_2$ transition in the $BaHfO_3$ matrix is observed for the first time as a dominant line and to be particularly useful as a red-light-emitting phosphor. Furthermore, we have also described (i) sintering of the resulting matrix at 900 °C and (ii) that emission of Eu-doped $BaHfO_3$ lattice was obtained at lower temperatures than other host lattices known in the literature.[25,26,28] Investigations along these lines are currently underway. In the near future, we intend to expand our research to other Group 4 metals.

ASSOCIATED CONTENT

Supporting Information. Full crystallographic data, FT-IR spectra, N_2 adsorption−desorption isotherms, Brunauer−Emmett−Teller (BET) surface area plot, Barrett−Joyner−Halenda (BJH) desorption, dV/dD, pore volume. This material is available free of charge via the Internet at http://pubs.acs.org.

AUTHOR INFORMATION

Corresponding Author

*E-mail: e-mail:plas@wchuwr.pl.

ACKNOWLEDGMENT

The authors would like to express their gratitude to the Ministry of Science and Higher Education (Grant No. N N204 340 437 and N N209 027 940) for financial support. We would also like to thank Dr. Wojciech Bury and Prof. Janusz Lewiński (Department of Chemistry, Warsaw Technical University), for their assistance in the N_2 sorption measurements.

REFERENCES

(1) Bohndorf, K.; Imhof, H.; Lee Pope, T., Jr. *Musculoskeletal Imaging: A Concise Multimodality Approach*; Georg Thieme Verlag: Stuttgart, Germany and New York, 2001.
(2) Duclos, S. J. *Electrochem. Soc. Interface* **1998**, 34.
(3) Thomas, J. K.; Padma Kumar, H.; Prasad, V. S.; Solomon, S. *Ceram. Int.* **2011**, *37*, 567.
(4) Zhang, J. L.; Evetts, J. E. *Mater. Lett.* **1993**, *15*, 331.
(5) Zhou, B.-Z.; Zhou, G.-H.; An, L.-Q.; Zhang, G.-J.; Wang, S.-W. *Ceram. Int.* **2009**, *35*, 2521.
(6) Turova, N. Y.; Turevskaya, E. P.; Kessler, V. G.; Yanovskaya, M. I. *The Chemistry of Metal Alkoxides*; Kluwer Academic Publishers: Boston, MA, 2002.
(7) Bradley, D. C.; Mehrotra, R. C.; Rothwell, I. P.; Singh, A. *Alkoxo and Aryloxo Derivatives of Metals*; Academic Press: London, 2001.
(8) Mehrotra, R. C.; Singh, A. Recent Trends in Metal Alkoxide Chemistry. In *Progress in Inorganic Chemistry*; John Wiley & Sons, Inc.: Hoboken, NJ, 2007.
(9) Veith, M.; Mathur, S.; Huch, V.; Decker, T. *Eur. J. Inorg. Chem.* **1998**, 1327.
(10) Veith, M.; Mathur, S.; Huch, V. *Inorg. Chem.* **1997**, *36*, 2391.
(11) Veith, M.; Mathur, S.; Huch, V. *Inorg. Chem.* **1996**, *35*, 7295.
(12) Labrize, F.; Hubert-Pfalzgraf, L. G.; Daran, J.-C.; Halut, S.; Tobaly, P. *Polyhedron* **1996**, *15*, 2707.
(13) John, Ł.; Utko, J.; Szafert, S.; Jerzykiewicz, L. B.; Kępiński, L.; Sobota, P. *Chem. Mater.* **2008**, *20*, 4231.
(14) Sobota, P.; Drąg-Jarząbek, A.; John, Ł.; Utko, J.; Jerzykiewicz, L. B.; Duczmal, M. *Inorg. Chem.* **2009**, *48*, 6584.
(15) Oxford Diffraction. *CrysAlis CCD and CrysAlis RED, Versions 1.171.33*; Oxford Diffraction Poland: Wroclaw, Poland, 2009.
(16) *SHELXTL, Version 6.14*; Bruker AXS, Inc.: Madison, WI, 2003.
(17) Clayden, J. *Nat. Chem.* **2010**, *2*, 523.
(18) Turova, N. Yu.; Turevskaya, E. P.; Kessler, V. G.; Yanovsky, A. I.; Struchkov, Y. T. *J. Chem. Soc., Chem. Commun.* **1993**, 21.

(19) Thomas, J. K.; Kumar, H. P.; Prasad, V. S.; Solomon, S. *Ceram. Int.* **2011**, *37*, 567.

(20) Lavat, A. E.; Baran, E. J. *Vib. Spectrosc.* **2003**, *32*, 167.

(21) Zheng, W.; Pang, W.; Meng, G. *Mater. Lett.* **1998**, *37*, 276.

(22) Ji, Y.; Jiang, D. Y.; Chen, J. J.; Qin, L. S.; Xu, Y. P.; Feng, T.; Shi, J. L. *Opt. Mater.* **2006**, *28*, 436.

(23) Dhoble, S. J.; Dhoble, N. S.; Pode, R. B. *Bull. Mater. Sci.* **2003**, *26*, 377.

(24) Liu, X.; Wang, X. *Opt. Mater.* **2007**, *30*, 626.

(25) Dobrowolska, A.; Zych, E. *Chem. Mater.* **2010**, *22*, 4652.

(26) Dobrowolska, A.; Zych, E. *Z. Kristallogr. Suppl.* **2009**, *30*, 367.

(27) Huang, J.; Zhou, L.; Wang, Z.; Lan, Y.; Tong, Z.; Gong, F.; Sun, J.; Li, L. *J. Alloys Compd.* **2009**, *487*, L5.

(28) Blasse, G.; Grabmeier, B. C. *Luminescent Materials*; Springer—Verlag: Berlin, 1994.